

# Crustal and upper mantle structure in the intracratonic Paraná Basin, SE Brazil, from surface wave dispersion using genetic algorithms

Meijian An<sup>a,b</sup>, Marcelo Assumpção<sup>a,\*</sup>

<sup>a</sup> Department of Geophysics, IAG, University of São Paulo, Rua do Matão 1226, 05508-090 São Paulo, SP, Brazil

<sup>b</sup> Laboratory Computational Geodynamics, Graduate University, Chinese Academy of Sciences, Beijing, China

Received 1 April 2004; accepted 1 December 2005

## Abstract

The mechanisms for the formation of intracratonic basins remain a matter of dispute. More information about deep crustal structures, especially in the poorly known intracratonic Paraná Basin, may contribute to a better understanding of their origin. A high-gravity anomaly along the basin axis has been suggested as due to a high-density lower crust caused by underplating. To test this hypothesis, S-wave velocity profiles in the Paraná Basin were studied using interstation surface wave phase velocities. Ps–P time differences from receiver functions were used as constraints to select models with good fit. Genetic algorithms (GA) were used to find the best fitting model and the range of acceptable models. A trial-and-error jumping iteration was developed to improve the GA inversion efficiency. The average S-wave velocities of the lower crust are less than approximately 3.8 km/s, lower than the global average of 4.0 km/s for platform areas. Near the basin center, where flood basalt thickness is maximal, similar low S-wave velocities were found, suggesting that underplating was not significant or widespread in the Paraná Basin and that a high density layer in the lower crust cannot be used to explain the high-gravity anomaly at the basin axis. No significant difference could be detected in the upper mantle between the axis and the border of the basin. The average upper mantle S-wave velocity is 4.65 km/s, a typical value for cold platform areas.

© 2006 Elsevier Ltd. All rights reserved.

**Keywords:** Crustal structure; Phase velocity; Surface wave; Genetic algorithm

## 1. Introduction

The Paraná Basin, one of the three major intracratonic basins in eastern South America (Fig. 1), has a fairly well-known stratigraphy (e.g. Zalán et al., 1990; Milani and Ramos, 1998), but the exact mechanism for its initiation and evolution remains a matter of speculation. Different models have been proposed to explain the origin and large-scale subsidence of intracratonic basins. For one class of models, the subsidence represents a passive response to processes outside the basin, such as flexural stresses caused by nearby orogenies or vertical motions of the lithosphere induced by upper mantle convection. Alternatively, models with local tectonism usually involve extensional/thermal processes and subsequent isostatic/cooling subsidence and often include some kind of

crustal loading by magmatic intrusions, phase densification, or underplating (e.g. White and McKenzie, 1989).

Relatively high Bouguer gravity anomalies characterize the present axis of the basin compared with its flanks (Ussami et al., 1993; Vidotti et al., 1998), as shown in Fig. 1a, and have been interpreted as due to a high-density lower crust, possibly caused by magmatic underplating (Molina et al., 1989). The average crustal thickness in the Paraná Basin was estimated by Assumpção et al. (2002) to be approximately 42 km, thicker than the surrounding high topography areas of the Brasília belt and São Francisco Craton. Isostatic requirements imply a higher density lithosphere beneath the Paraná Basin (Assumpção et al., 2002), which would be compatible with lower crust densification. However, no deep crustal studies have been carried out to test the interpretation of lower crustal densification or underplating.

Previous investigations of deep crustal structures in the Paraná Basin used surface waves along two different interstation paths from the basin center to its edges (Fig. 1b) and found an average crustal thickness of 42 km, with the lithosphere at least 150 km thick (Snoko and James, 1997; Snoko and Sambridge, 2002). The shallow sedimentary layers (studied by An and Assumpção, 2005) have an average S-wave velocity of

\* Corresponding author. Tel.: +55 11 30914755; fax: +55 11 30915034.

E-mail addresses: meijianan@yahoo.com.cn (M. An), marcelo@iag.usp.br (M. Assumpção).

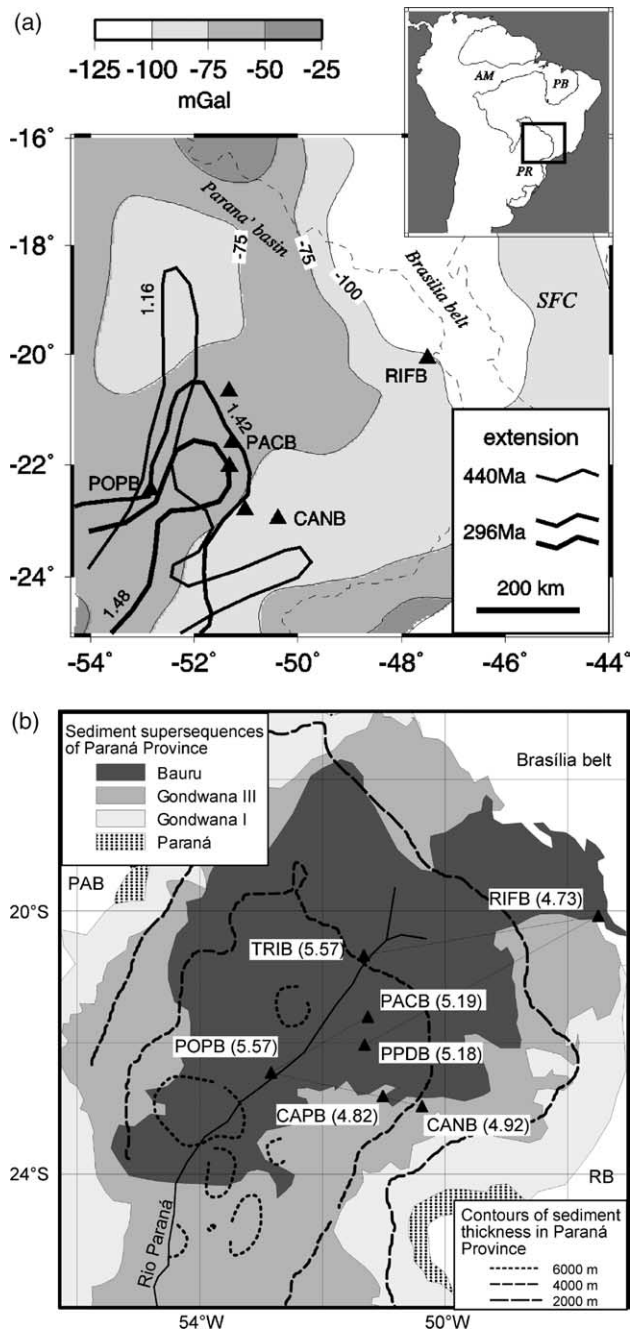


Fig. 1. (a) Bouguer gravity map showing relatively high anomalies along the basin axis. Gravity data are from Ussami et al. (1993). Contour lines denote values of the stretching factor  $\beta$  (Quintas et al., 1999). The  $\beta$  contour 1.16 refers to the initial basin subsidence at 440 Ma; the contours 1.42 and 1.48 refer to the 296 Ma subsidence. Triangles are the stations used in this work. SFC, São Francisco Craton. The inset shows the three major intracratonic basins of the South American platform: Amazon (AM), Parnaíba (PB), and Paraná (PR). (b) Simplified geological map with station pairs. Triangles are stations labeled with station name and the observed Ps–P time difference from receiver functions (Assumpção et al., 2002; França, 2003). Geological supersequences are from Milani and Ramos (1998) and contours of sediment thickness from Bizzi et al. (2001). PAB, Paraguay–Araguaia belt; RB, Ribeira belt.

approximately 2.7 km/s and an average depth of 2.5–3 km in the area of Fig. 1. Assumpção et al. (2002) used receiver functions to estimate crustal thicknesses in SE Brazil without a detailed study of seismic velocities beneath each station. Herein, we

Table 1  
Summary results from receiver function analysis

Station	Ps–P (s)	Vp/Vs
CANB	$4.92 \pm 0.36$	$1.74 \pm 0.03$
CAPB	$4.82 \pm 0.12$	$1.73 \pm 0.02$
PACB	$5.19 \pm 0.17$	$1.72 \pm 0.02$
POPB	$5.57 \pm 0.15$	Undeterminable
PPDB	$5.18 \pm 0.14$	$1.85 \pm 0.05$

study the lithospheric structure along two short paths near the basin axis by inverting new observations of interstation phase velocities constrained with Ps–P time differences from receiver functions (Table 1). We also develop and apply an improved genetic algorithm method in the inversion.

## 2. Basin evolution

The Paraná Basin is filled with sedimentary and volcanic sequences of Ordovician–Cretaceous age (Milani and Ramos, 1998): Rio Ivaí (Caradocian–Llandoveryan), Paraná (Lochkovian–Frasnian), Gondwana I (Westphalian–Scythian), Gondwana II (Anisian–Norian), Gondwana III (Late Jurassic–Berriasian), and Bauru (Aptian–Maastrichtian). It is surrounded by late Proterozoic–early Paleozoic foldbelts (e.g. Brasília belt and Paraguay–Araguaia belt, respectively) of the Brasiliano/Pan-African orogen, which was the last major tectonic event to amalgamate all crustal blocks into the present configuration in Brazil (Almeida et al., 2000). On the basis of radiometric dates from two basement samples, a Proterozoic ‘cratonic’ nucleus was inferred beneath the Paraná Basin (Cordani et al., 1984; Brito Neves and Cordani, 1991). Generally, high P- and S-wave velocities found at lithospheric depths in the central part of the basin (Schimmel et al., 2003) are consistent with a cratonic nucleus. The Paraguay–Araguaia and Brasília belts mark the final collision of this ‘nucleus’ with the Amazon and São Francisco cratons, respectively (Fig. 1b). However, Milani and Ramos (1998) point out that the central part of the basin has a rift zone (determined by shallow geophysical data), as well as early igneous activity, which are not consistent with a stable cratonic nucleus.

The basin started to develop in the Early Paleozoic after the Brasiliano orogen. The initial Ordovician subsidence ( $\sim 440$  Ma) has been attributed to cooling of the whole region after the Brasiliano orogen (Zalán et al., 1990). However, we might expect a higher cooling effect along the surrounding foldbelts, directly involved in the Brasiliano orogen, and a smaller thermal effect near the possible ‘cratonic’ center of the basin. Another important subsidence stage occurred in Carboniferous–Permian times (starting  $\sim 296$  Ma). Both these subsidence phases could be interpreted as due to a small degree of crustal stretching concentrated near the axis of the basin (Quintas, 1995; Quintas et al., 1999), as shown in Fig. 1a. The 440 Ma subsidence would have caused a stretching factor  $\beta$  of at most 1.16; the subsidence at 296 Ma would have caused  $\beta$  values of at most 1.48 (Fig. 1a). Alternatively, the basinwide subsidence of the Carboniferous–Permian stage could be attributed to a mantle flow effect induced by deep

subduction processes at the SW border of Gondwana (Pysklywec and Quintas, 2000).

Milani and Ramos (1998) correlate the main subsidence cycles of the basin with the main orogenic phases of the nearby subduction of the Panthalassa oceanic lithosphere and interpret the initial Paraná Basin as a wide flexural foreland basin caused by orogenic load at the SW border of the Gondwana supercontinent. Upper mantle flow induced by the Panthalassa subduction zone also could induce various phases of subsidence/sedimentation and uplift/erosion (Pysklywec and Quintas, 2000). However, a high-density layer in the lowermost crust is commonly observed in many continental rift basins (e.g. Mooney et al., 1983, 2001). For this reason, high-gravity anomalies along basin axes are often interpreted as magmatic intrusions, such as in the Amazon Basin (Nunn and Aires, 1988), or as underplating, as in the Paraná Basin (Molina et al., 1989).

Extensive continental flood basalt was extruded on most of the Paraná Basin from 137 to 130 Ma, just prior to the South Atlantic rifting. The basalt layers, the Serral Geral Formation of the Gondwana III supersequence, reach their maximum thickness of approximately 1.5 km near the basin center (near station POPB in Fig. 1). The South Atlantic rifting and basalt flow commonly are associated with the Tristan da Cunha mantle plume (e.g. White and McKenzie, 1989). Extensive partial melting in the upper mantle, necessary to produce the voluminous basalt flow, would likely be accompanied by magmatic intrusions of the lower crust or underplating.

The depocenter of the Bauru supersequence is roughly coincident with the area of maximum basalt thickness (Fig. 1b). The basin subsidence may have continued until Upper Cretaceous times, with the Bauru sediments occupying the flexural sag caused, perhaps, by the basalt overload (Zalán et al., 1990; Milani and Thomaz Filho, 2000) or by cooling of magmatic intrusions in the deep crustal or upper mantle. Clearly, studies of the deep crustal structure are important to verify the various proposed hypotheses for the subsidence mechanism and evolution of the Paraná Basin.

### 3. Surface wave data

Fig. 1 shows the temporary broadband seismic stations used in this study, which were part of the Brazilian Lithosphere

Seismic Project (BLSP). The stations used three-component STS-2 sensors with flat velocity response from 0.008 to 50 Hz. The two longer paths, RIFB–TRIB and RIFB–PPDB, had been used by Snoke and James (1997) and Assumpção et al. (2002). The two shorter paths, POPB–PACB and POPB–CANB, are used here to estimate more localized crustal structures.

Teleseismic events (Table 2) were selected with a propagation path no more than 5° off the great circle between the stations. Preliminary surface wave group velocities were determined by multiple filtering (Dziewonski et al., 1969; Herrmann, 1973, 1987; Bhattacharya, 1983). These initial velocities were used to isolate the fundamental mode surface waves using a phase-matched filter (Herrin and Goforth, 1977; Herrmann, 1987; Levshin et al., 1998), which removes interfering, scattered body waves and higher-mode surface waves. Fig. 2 shows an example of two original, instrument-corrected seismograms, together with the fundamental mode waves isolated by the phase-matched filter, of the Rayleigh waves from event 2001184 (Table 2), which propagate along the POPB–CANB path. The filtered traces were cross-correlated to obtain the interstation phase velocities using the seismological program V3.15 (Herrmann, 2001; Herrmann and Ammon, 2002).

Fig. 3 shows the observed interstation phase velocities of the two POPB paths (POPB–CANB and POPB–PACB), together with the mean values used in the inversion. The error bars for the average phase velocities were taken as the standard deviation of the mean. For periods with only one or two observations, larger uncertainties were assigned.

### 4. Receiver functions

Receiver functions for all stations in the Paraná Basin were calculated by frequency domain deconvolution by Assumpção et al. (2002), as well as by time-domain deconvolution using the codes given by Ligorria and Ammon (1999). The two techniques give similar time delays for the P–S Moho conversion (Ps phase). Fig. 1b and Table 1 show the observed Ps–P time differences ( $\Delta T \pm \sigma_{\Delta T}$ ), corrected for vertical incidence, for the stations used in this study (Assumpção et al., 2002; França, 2003). The uncertainties represent the standard deviation from different back-azimuths and reflect lateral variations beneath the station. The multiply reflected phase

Table 2  
Events used for interstation phase velocities

YYYYDDDD	UT	Lat.	Long.	Depth (km)	Magnitude	Dist. (°)	Baz (°)
POPB–PACB							
2002143	15:52:15.4	–30.734	–71.231	52	5.8	20.07	239.0
2002144	00:23:16.0	–31.966	–70.954	61	5.3	20.35	235.4
2002163	19:52:47.1	–0.655	–20.667	10	5.0	36.38	59.1
2002169	13:56:22.4	–30.754	–70.964	53	6.0	19.87	238.7
2002174	11:10:42.1	–30.801	–71.034	67	5.7	19.94	238.6
POPB–CANB							
2000216	19:22:10.8	–17.538	–71.587	33	5.4	20.61	281.3
2001111	13:09:19.5	–13.525	–76.670	39	5.1	26.64	286.1
2001177	04:18:31.6	–17.739	–71.342	33	6.7	20.33	281.0
2001184	12:57:41.8	–16.510	–73.747	29	5.0	22.90	282.1

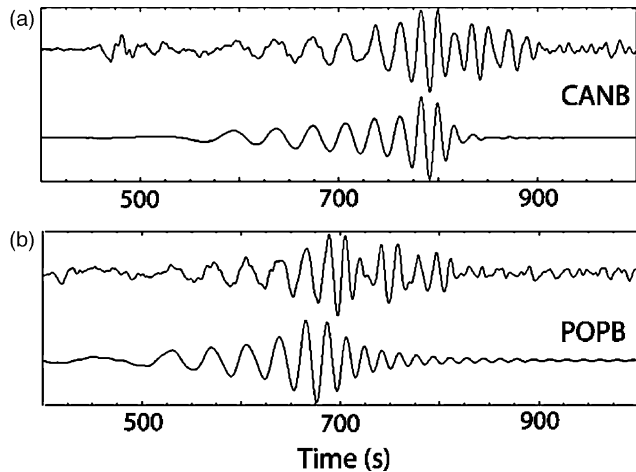


Fig. 2. Vertical components of event 2001184 (Table 1) recorded at (a) CANB and (b) POPB. The diagram shows (top) the original instrument-corrected displacement and (bottom) the match-filtered trace.

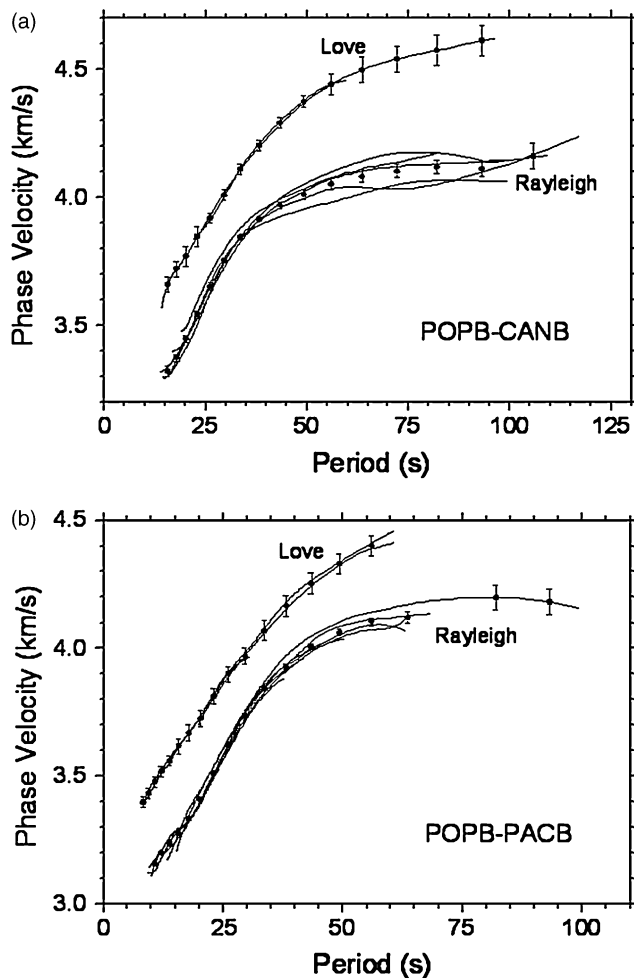


Fig. 3. Observed surface wave phase velocities: (a) POPB-CANB and (b) POPB-PACB. The curves are the observed dispersions of each earthquake from Table 2; the mean of the observed data are shown as circles with error bars and were fitted in the inversion.

P2ps (also called PpPms) can be used to estimate the average crustal  $V_p/V_s$  ratio but is a weak signal, less robust and more dependent on the parameters used in the deconvolution procedure. Slant stacking of receiver functions, using França and Assumpção's (2004) technique, was used to enhance the P2ps phase, which enables  $V_p/V_s$  ratios for most stations to be estimated (Table 1). Data for station POPB do not show any recognizable multiple phases to enable an estimate of the  $V_p/V_s$  ratio.

## 5. Inversion method

### 5.1. Genetic algorithm and surface waves

The inversion of surface wave dispersion is a nonlinear problem and can be carried out with linearized least squares methods (e.g. Herrmann, 1987; Snoko and James, 1997). Global search methods, such as genetic algorithm (GA), are also used (e.g. Lomax and Snieder, 1994, 1995; Shi and Jin, 1996; Yamanaka and Ishida, 1996; Zhang et al., 1998; Du et al., 2002). Yamanaka and Ishida (1996) argue that GA-based inversion methods are more stable than gradient-based (linearized) methods. Lomax and Snieder (1994, 1995) apply simple GA (SGA) to search all acceptable models. Many studies have used SGA to map all acceptable models but not find the best ('optimized') model, because SGA is efficient for searching the optimal solutions in simple problems but unsuitable for optimizing the solution in complex problems. For example, SGA is efficient to invert for S-wave velocities in a model with few layers but less efficient for more parameters, such as thickness and S velocity. This difficulty is caused mainly by the complex trade-offs among parameters, such as that between thickness and S-wave velocity, which require much more search work. Shi and Jin (1996) manually analyze the distribution of all model parameters to restrict the search ranges iteratively and show that SGA can find the best solution in a complex model space of surface wave dispersion inversion. However, this solution came at the expense of losing the range of acceptable models. Yamanaka and Ishida (1996) choose the final model by averaging the final parameters of 20 GA runs.

To find simultaneously the best model (global misfit minimum) and the range of acceptable models, some GA parameters must be adjusted according to the problem complexity, such as using an appropriate population size (Schaffer et al., 1989; Goldberg et al., 1992; Deb, 1998). Furthermore, GA can be improved to provide quality solutions more efficiently through hybridization (Goldberg and Voessner, 1999). In this study, we use a simple and efficient trial-and-error jumping iteration to hybridize SGA to improve the model optimization.

Because of the strong trade-off among parameters, the inversion of receiver functions or surface wave dispersion alone is often ill posed. Surface waves depend on depth-averaged S-wave velocities, whereas receiver functions sample vertical travel times and velocity contrasts at crustal interfaces. For this reason, the joint inversion of surface wave and receiver

function data is more stable (Özalaybey et al., 1997; Du and Foulger, 1999; Julià et al., 2000). However, interstation phase velocities represent average values over paths a few hundreds of kilometers long, whereas receiver functions sample more localized crustal properties beneath a single station. Quite often, lateral variations cause receiver functions from different azimuths, obtained at the same station, to differ. Therefore, it is not always clear how to interpret the models that result from the combination of detailed local information from receiver functions and average properties in a long profile. For this reason, we use only the average Ps–P time difference obtained at the stations along the surface-wave path.

5.2. Objective functions

We want to find the horizontal plane-layer models that best fit our phase velocity observations. In the direct problem, the phase velocities were calculated following the routine of Lomax and Snieder (1995). The misfit of the surface wave dispersion,  $Q_v$ , is defined as

$$Q_v = \sqrt{\frac{\sum_{i=1}^n [5(V_i^o - V_i^c)^2 / \sigma_i^2 - 4D_i^2 / \sigma_i^2]}{\sum_{i=1}^n [1/\sigma_i^2]}} \tag{1}$$

where  $n$  is the number of observations;  $V_i^o$  and  $V_i^c$  are the observed and calculated phase velocities, and  $\sigma_i$  is the observation error of  $V_i^o$ ; and  $D_i$  is the smaller of  $|V_i^o - V_i^c|$  and  $\sigma_i$ . This objective function is similar to a weighted rms misfit if all  $|V_i^o - V_i^c| < \sigma_i$ . However, a calculated phase velocity outside the range of observational error has a larger contribution to the misfit, which forces solutions to stay within the error bounds.

We want to estimate not only the S-wave average velocities between two stations but also the depths to the main interfaces, such as the Moho discontinuity. For this reason, we use only five layers—sedimentary layer, upper crust, lower crust, lithospheric mantle (lid), and asthenosphere (half-space below the lithosphere)—and invert for both S-wave velocity and thickness.

Examination of the misfit landscape (modality) can indicate important properties of the inversion problem. An example of misfit modality for a synthetic five-layer model appears in Fig. 4. We added perturbations to the S-wave and thickness of the third layer (lower crust), as we show in Fig. 4a, and contoured the misfit between the perturbed dispersion and the original model (gray pattern in Fig. 4b).

The Ps–P time difference ( $\Delta T$ ) offers an additional constraint. The Ps–P misfit function,  $Q_{\Delta T}$ , is defined as  $Q_{\Delta T} = |2 \times |\Delta T_o - \Delta T_c| - D_{\Delta T}|$ , where  $\Delta T_o$  and  $\Delta T_c$  are the observed and calculated values, respectively;  $D_{\Delta T}$  is the smaller of  $|\Delta T_o - \Delta T_c|$ , and  $\sigma_{\Delta T}$ ;  $\sigma_{\Delta T}$  being the observation error of  $\Delta T_o$ . In this definition, a model with Ps–P inside the error range will have  $Q_{\Delta T} = |\Delta T_o - \Delta T_c|$ ; otherwise, the misfit will be twice as large ( $2|\Delta T_o - \Delta T_c|$ ). This requirement penalizes models with a misfit outside the observed error bounds.

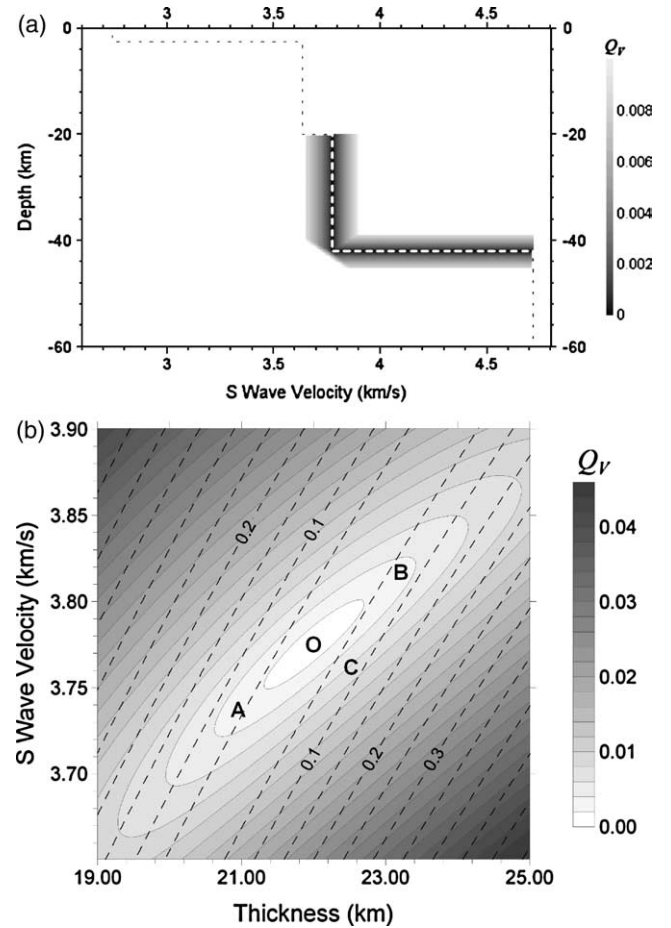


Fig. 4. A synthetic model and its perturbations. (a) The synthetic model (dashed line) and the good (misfit  $Q_v < 0.01$  km/s) perturbed models (shaded in grayscale) of misfit of Love and Rayleigh phase velocities. (b) The misfit of Love and Rayleigh phase velocities (shaded in gray scale) and the Ps–P error (dashed lines) as a function of thickness, and S-velocity of the third layer of the synthetic model. O is the synthetic model; A–C are discussed in the text.

In the misfit landscape (Fig. 4b), the valleys of the Ps–P data and the phase velocity data are roughly parallel, which means that including the Ps delay as an additional constraint will not completely eliminate the velocity/thickness trade-off. However, using two different sets of data, especially in the presence of noise, may help stabilize the inversion and place the combined minimum misfit closer to the ‘true’ model. We selected the sum of weighted objective functions as the optimization objective function ( $Q$ ) (Eq. (2)), where  $w$  is a constant weight:

$$Q = Q_v + w \cdot Q_{\Delta T} \tag{2}$$

6. GA hybridization

Strong trade-off between parameters is a frequent and serious problem causing inversion instabilities. In nonlinear global search methods, it may prevent reaching the minimum with enough accuracy and can decrease the efficiency of a random algorithm like SGA. For example, in Fig. 4b, models A

Table 3  
Search ranges for the HGA test

Layer	Thickness (km)	Vs (km/s)
Sediments	1.5–7	1.5–3.5
Upper crust	1–40	3.0–4.0
Lower crust	1–40	3.0–4.5
Upper mantle lid	30–90	3.5–6.0
Half-space	–	3.5–6.0

and B have similar misfits but are very different, whereas model C has a larger misfit ( $Q_V$ ) despite being closer to the true model (global minimum  $O$ ) and may not survive to the next generation. If sampling of the model space is not dense enough, the inversion incorrectly may indicate a multisolution. Because random search algorithms do not usually recognize local gradient, it is very easy to be misled from C to a ‘better’ model like A, which moves away from the global solution.

Therefore, we hybridized the GA with a local trial-and-error jumping iteration. In each generation, the good models (less misfit than the average misfit) are perturbed by changing their parameter vector in a random direction. If the initial perturbation vector, with a small amplitude (distance from the starting model), makes the misfit worse, the perturbation is changed to the opposite direction. Then the perturbation amplitude (jump interval) increases exponentially (doubles for each trial) until the model stops improving. This local iteration improves the GA efficiency near the optimum region.

The efficiency of this hybridized genetic algorithm (HGA) was tested using the objective function of Eq. (1) to fit the phase velocities of the synthetic model in Fig. 4 for the same periods shown in Fig. 3a. All the observation errors ( $\sigma_i$ ) were set to a large constant. The search ranges for the five layers are shown in Table 3.

Crossover probability was 0.80, and mutation probability was 0.02. String length was 5, which means that each parameter was sampled at an interval of 1/64th of its range. Table 4 and Fig. 5 compare the average results of five runs of HGA and SGA. For the HGA, initial perturbation amplitudes were tried with 5 and 8 parameter intervals; HGA fits the data better using fewer model computations than SGA. Tests also were performed to determine the effects of different string lengths and initial jump amplitude (Table 5); HGA again offers better performance and is less sensitive to the initial models, population size, and search precision than SGA.

This advantage, less sensitivity to the initial models, is important because GA results may depend on the initial model population, which can make it stick around a local minimum in a misfit landscape in one run. Because it is less sensitive to the

precision of the searched model, HGA can be used in more accurate model searching. The local iteration also can increase the diversity of acceptable models near the optimal region. Although HGA is superior to SGA, it should be run several times; some acceptable regions may be missed by limited searches in problems with a large model space.

## 7. Inversion result

In inverting the shallow structure using group velocity observations, An and Assumpção (2005) show that strong lateral heterogeneities along the path can cause instabilities in the inverted S-velocity profile. The comparison of results using different model parameterizations is recommended to test for heterogeneity, and we adopt the two inversion modes suggested by An and Assumpção (2005).

In mode 1 (inversion for S-velocity and thickness), the inverted model is composed of five layers: sedimentary, upper crust, lower crust, lithospheric lid, and asthenosphere. The search ranges (thickness, Vs) are as follows: sedimentary (1.5–7 km, 2.4–2.8 km/s), upper crust (5–40 km, 2.5–4 km/s), lower crust (1–40 km, 3.0–4.5 km/s), lid (1–150 km, 3.5–6.0 km/s), and asthenosphere (half-space, 3.5–6.0 km/s). In mode 2 (inversion for S-velocity with fixed layer thicknesses), the model is composed of five crustal layers and several mantle layers (see Figs. 6 and 7). In the crust, the uppermost layer (sedimentary) is 2.7 km thick, and the other four layers are 10 km each. The velocity ranges are similar to those of mode 1.

In the GA process, after an initial evaluation of the good models in the first few generations, the search ranges are reduced to optimize the process, as suggested by An and Shi (1996), and the GA iterations are continued. Four different weights ( $w = 0.0, 0.0033, 0.0067, \text{ and } 0.0167$ ) in the objective function (Eq. (2)) were used in the inversion. For each weight, more than 15 runs were carried out, and all good models were saved. The use of several different weights in Eq. (2) is necessary to make the search cover the model space as widely as possible. The combined objective function,  $Q$  in Eq. (2), helps indicate solutions that fit both sets of data (dispersion and Ps–P) but does not guarantee that all these good models will fit both data sets equally well. For this reason, additional criteria to select good solutions are needed, such as selecting small  $Q_V$  or small  $Q_{\Delta T}$ .

### 7.1. RIFB paths

We first used our HGA method with the dispersion data from the longer paths RIFB–TRIB and RIFB–PPDB, sampling the average lithospheric properties from the basin center to its

Table 4  
Optimal results of SGA and HGA with string lengths of 5

	Population size	Number of generations	Intervals of initial jump	Average number of evaluated models	Best model’s misfit	Average misfit of best models in five runs
SGA	40	500	0	20000	0.0086	0.0234
HGA	25	250	5	18399	0.0049	0.0081
			8	17645	0.0076	0.0095

Note. The GA was run five times with each parameter setting.

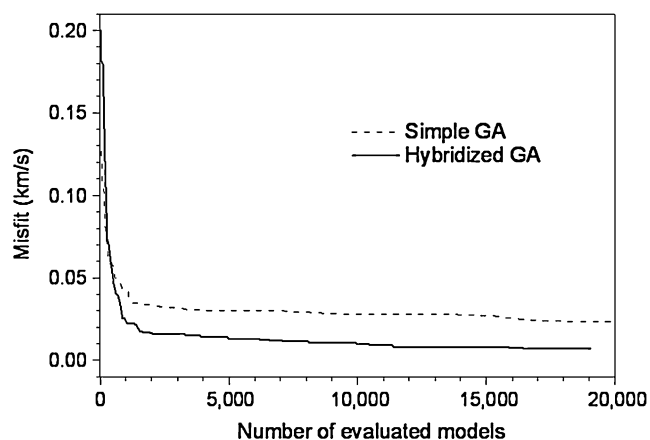


Fig. 5. Misfit of the best model as a function of the evaluated model number to compare the efficiency of HGA and SGA. Each line is the average of five runs. The inversion settings are those of Table 4 with HGA having initial jump amplitude of eight parameter intervals.

edge. This data set (Fig. 6c) had been inverted previously with linearized least square inversion (LLSI) (Snoke and James, 1997; Assumpção et al., 2002) and neighbor algorithm (NA) (Snoke and Sambridge, 2002). We used the same fixed  $V_p/V_s$  ratios of Snoke and James (1997): 1.8 for the sedimentary layer, 1.73 for the upper and lower crust, and 1.78 for the upper mantle.

All models of our inversion with misfit  $Q_V < 0.025$  km/s are shown in Fig. 6 (misfit in gray scale) in comparison with the LLSI (Snoke and James, 1997; Assumpção et al., 2002) and NA (Snoke and Sambridge, 2002) results. The white dashed lines in Fig. 6a, b, and d are the fitness-weighted average velocity profile of our HGA inversion (fitness is the reciprocal of the misfit  $Q_V$ ). The white solid lines show the LLSI and NA results, which are almost the same. Despite small differences in the misfit definition and model parameterization, the final results are very similar. Fig. 6b shows the models, which have misfit  $Q_V < 0.025$  km/s and fit the average Ps–P times for the two RIFB paths to within 0.1 s. Velocities of the lower crust and the Moho depth are better defined. The previous LLSI model had the sedimentary layer fixed with thickness of 2.6 km and S-velocity of 2.7 km/s; the interface between upper and lower crust had been arbitrarily fixed at 20 km depth. Our results suggest that the upper crust may be slightly thicker and the lower crust slightly thinner. The upper mantle shows a slight trend of

decreasing S-wave velocities but probably not too significant, as already concluded by Snoke and Sambridge (2002).

We also inverted the data of Fig. 6c using more layers with fixed thicknesses (inversion mode 2). The thickness of the sedimentary layer was fixed at 2.7 km, the other crustal interfaces were set at 10 km intervals, and thicker layers were used in the upper mantle. No smoothing was applied. The results (Fig. 6d) show the same general trend in the crust as in Fig. 6a and b but also strong instabilities in the upper mantle. Although errors in dispersion velocities are a common cause of such instabilities, An and Assumpção (2005) show that lateral structure variation also can cause inversion instabilities. The longer paths from station RIFB probably sample different crustal and upper mantle structures between the center of the basin and its margins, contributing to such instabilities.

## 7.2. POPB–PACB path

For the POPB–PACB path, the average Ps–P time ( $5.31 \pm 0.10$  s) observed at stations POPB, PPDB, and PACB (Table 1) was taken as an observation ( $\Delta T_o \pm \sigma_{\Delta T}$ ). Initially, the GA inversion started with a fixed  $V_p/V_s$  ratio of 1.73. After the optimization of the search ranges, the  $V_p/V_s$  of the whole crust was allowed to range from 1.70 to 1.90, according to the measured values for stations PACB and PPDB (Table 1). However, P-wave velocity is not well constrained by surface wave data, and the final accepted models have a wide variation in  $V_p/V_s$  ratios.

All the best models ( $Q_V < 0.02$  km/s) obtained with inversion mode 1 appear in Fig. 7a. Despite the wide range of  $V_p/V_s$  (not shown), the Moho depth is clearly defined for models with Ps–P error less than 0.1 s (Fig. 7c). Results for the fixed-thickness mode 2 appear in Fig. 7e. The white dashed lines show the fitness-weighted average and one standard deviation of the velocity profiles. Inversion mode 2 shows very similar average results, with little oscillation in the upper mantle velocities. This consistency implies that in this path, along the basin axis, lateral variations should not be too strong.

## 7.3. POPB–CANB path

A Ps–P value of  $5.11 \pm 0.18$  s (Table 1) was used for the inversions of the POPB–CANB path. The  $V_p/V_s$  ratios were allowed to vary from 1.70 to 1.90 in the sedimentary layer

Table 5  
Optimal results of HGA with population size of 15

Number of generations	String length	Intervals of initial jump	Average number of evaluated models	Best model's misfit	Average misfit of best models in five runs
250	5	5	9550	0.0081	0.0100
		8	9410	0.0080	0.0104
		10	9250	0.0085	0.0099
	8	5	12420	0.0052	0.0065
		8	11301	0.0052	0.0069
		10	10710	0.0038	0.0068
	12	5	16505	0.0053	0.0096
		8	15803	0.0065	0.0079
		10	15701	0.0024	0.0070

Notes. The GA was run five times with each parameter setting.

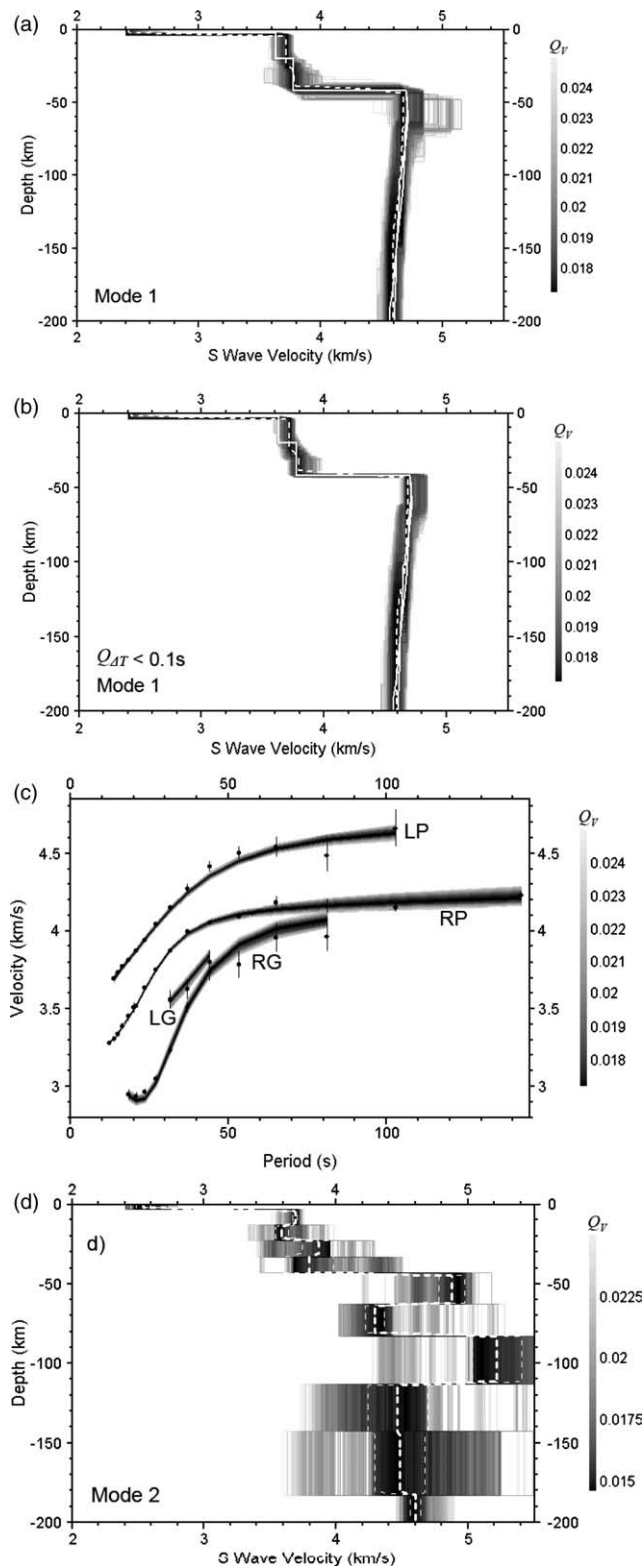


Fig. 6. Inversion of phase and group velocity data from the two RIFB paths, showing the best models in grayscale of misfit,  $Q_r$ . (a) Best models in inversion mode 1 (inverting for velocity and thickness of each layer). (b) Models selected from (a) with Ps–P error ( $Q_{\Delta T}$ ) < 0.1 s. In (a) and (b), the dashed white line is the fitness-weighted average S-velocity at each depth, and the white solid line is the inverted models by LLSI (Snoko and James, 1997) and NA (Snoko and Sambridge, 2002). (c) Data and modeled dispersions of (a). (d) Inversion mode 2 with more layers and fixed thicknesses; the thick dashed line is the average S velocity in each depth, and the thin dashes are two standard deviations.

and 1.70–1.78 in the upper and lower crust, according to the values for stations CAPB and CANB (Table 1). The inverted crustal velocities (Fig. 7b, d, and f) are approximately the same on average, though the upper crust seems to have a slightly higher velocity compared with the previous path (Fig. 7c). In the upper mantle, a thin lid with unrealistic high velocities was obtained with inversion mode 1, and strong oscillations were observed with fixed-thickness inversion mode 2. The Ps–P times along the POPB–CANB path (Fig. 1a, Table 1) show larger variations compared with the POPB–PACB, so more crustal heterogeneities are expected. Strong lateral variation along the interstation path can contribute to such oscillations (An and Assumpção, 2005).

To test whether the spurious high velocity lid just below the Moho may be an effect of lateral variations, synthetic dispersion data were calculated for a heterogeneous path composed of two different homogenous sections, shown in solid white lines in Fig. 8a. Each section (half the propagation path) has a different upper crustal velocity (3.4 and 3.5 km/s) and Moho depth (45 and 50 km). Fig. 8b shows the inversion of one of the homogeneous sections as an additional test of the HGA inversion method: Despite large scatter in the good models, the optimum model and average profile (dashed line) are very similar to the synthetic input model. The composed synthetic dispersion data (taken from the average slowness of the two sections) were inverted with the same HGA parameters, and the resulting models (gray lines in Fig. 8a) also show a trend of high velocities just below the Moho. The fitness-weighted average model (dashed line in Fig. 8a) retrieved the average velocity of the upper crust, but the lateral variation in crustal thickness caused an artificial high-velocity thin lid, which may explain the observed results in Fig. 7b and d. A similar but weaker effect has been observed in the inversion of the two RIFB paths, as seen in Fig. 6a and b.

To eliminate this effect in the top of the upper mantle, the lower limit of the search range for the thickness of the lithospheric lid was increased from 1 to 40 km; the new inversion results are shown in Fig. 9. The average S-velocity in the top 40 km of the upper mantle is now approximately 4.6 km/s. A trend of decreasing S velocities with depth (similar to the pattern observed for the two RIFB paths) may be suggested, but an interpretation in terms of the lithosphere/asthenosphere boundary should be avoided because of the possible lateral variation effects, as shown previously, as well as the depth resolution of our data set.

## 8. Discussion

Fig. 10 shows the misfit-weighted average S-velocity profiles of the three interstation inversions, constrained by Ps–P times. Because the longer paths (RIFBs, POPB–CANB) cross the basin center and border and sample larger lateral variations, their S-velocity models (dashed lines in Fig. 10) are less reliable than that of the shorter path (POPB–PACB), and only the general S-velocity trend can be interpreted.

For each of the three stations closer to the basin center (POPB, PACB, PPDB), An and Assumpção (2004) carried out

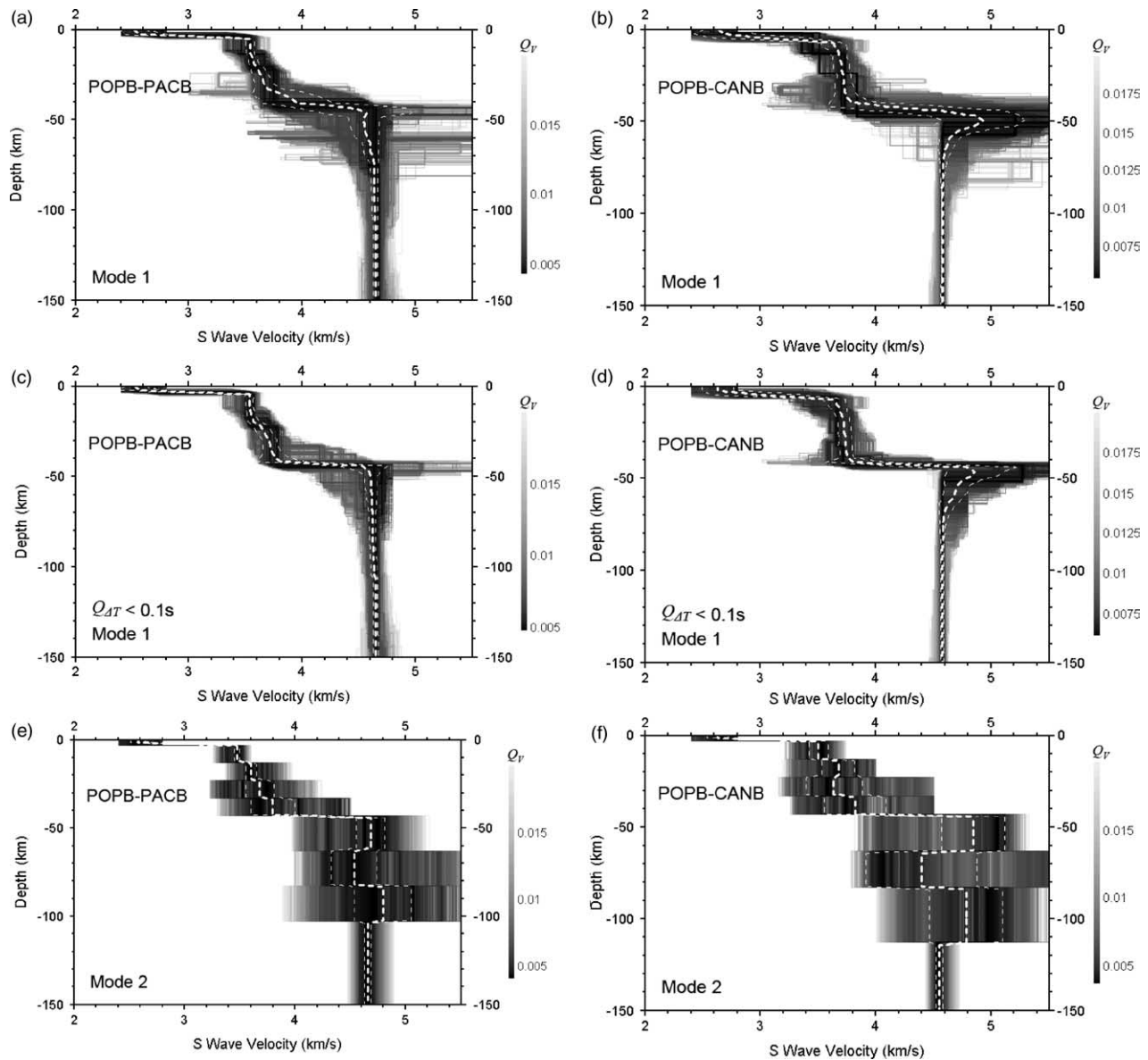


Fig. 7. The acceptable models in grayscale of misfit of the POPB–PACB and POPB–CANB paths. The thick white dashed line is the average S velocity at each depth, and the thin dashes are two standard deviations, calculated using the fitness (reciprocal of misfit  $Q_V$ ) as weight. Models in (c) and (d) have errors of Ps–P < 0.1 s.

a joint inversion of the receiver function waveform and phase velocities (with the data from path POPB–PACB, Fig. 3b) using layers with velocity gradients. The average of the three profiles of their joint inversion (thin solid line in Fig. 10) matches closely the results from the POPB–PACB interstation path presented here (thick solid line), as we expected. The only difference is a smoother Moho transition of the joint inversions necessary to match the amplitudes of the Ps conversions (An and Assumpção, 2004).

The average S-wave velocity in the top 100 km of the upper mantle is 4.65 km/s. Although a slight trend of higher velocities below 100 km depth may appear for the basin axis (solid lines) compared with the basinwide average profiles (dashed lines for RIFBs and POPB–CANB paths), this trend is probably not significant, given the range of acceptable velocities in the inverted profiles (Figs. 7 and 9).

In addition, the slight trend of decreasing velocities in the upper mantle in the basin-average profiles (dashed lines) may be an artifact created by lateral variation (Fig. 8). Therefore, we concentrate our interpretation in the crustal section only.

Average Moho depths are 40–45 km, consistent with previous crustal thickness estimates of 40–46 km using receiver functions (Assumpção et al., 2002). The S-velocities in the lower crust tend to be smaller than 3.8–3.9 km/s. The models for the longer paths are strikingly similar and show average properties of the basin over large areas from the center to the border. The short POPB–PACB profile, near the basin axis, differs slightly from the other two basin-average profiles (Fig. 10): A thicker upper crust is suggested with lower S-velocity (3.5–3.6 km/s) down to 25–30 km. Velocities in the lower crust reach, at most, 3.8 km/s.

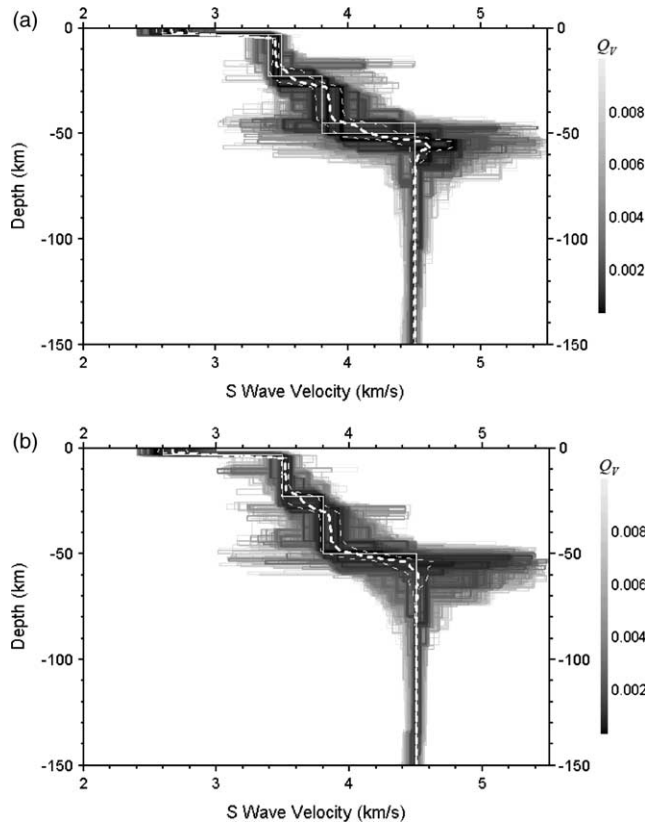


Fig. 8. The acceptable inverted models in grayscale of misfit. (a) Horizontal heterogeneous path composed of two homogeneous sections with different upper crustal velocities (3.4 and 3.5 km/s) and Moho depths (45 and 50 km). (b) One of the two homogeneous sections used to compose the heterogeneous path in (a). The white dashed line is the fitness-weighted average S velocity, and the white solid lines are the synthetic homogeneous sections.

A high velocity layer in the lowermost crust ( $V_p > 7.0$  km/s,  $V_s > 4.0$  km/s), up to 10 km thick, is often observed in large sedimentary basins and areas of continental rift and attributed to underplating (e.g. Mooney et al., 1983; Holbrook et al., 1992; Durrheim and Mooney, 1994). Molina et al. (1989) model a 25–30 mGal gravity high along the axis of the northern Paraná Basin as due to a high-density 12 km thick layer in the lowermost crust, interpreted as evidence of underplating (in

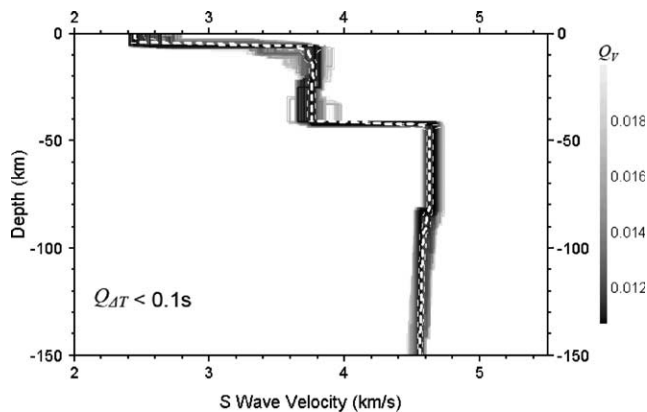


Fig. 9. The good inverted models in grayscale of misfit of POPB–PACB path. The minimum thickness of the lithospheric lid is 40 km. Other parameters are the same as in Fig. 7d.

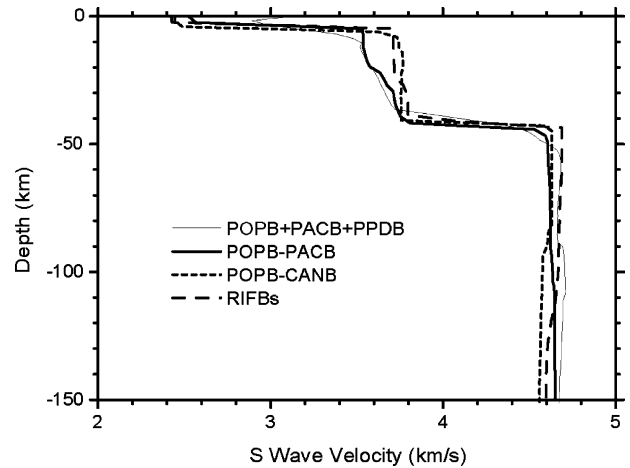


Fig. 10. The fitness-weighted average S-wave velocity of the inverted models of all three data sets, with the constraint of  $P_s$ – $P$  error  $< 0.1$  s. The result for RIFBs is taken from Fig. 6b, for POPB–PACB from Fig. 7c, and for POPB–CANB from Fig. 9. The thin solid line ‘POPB + PACB + PPDB’ is the average of the profiles beneath each station obtained by An and Assumpção (2004). Note that the two solid lines represent the structure near the basin center, whereas the two dashed lines represent the average structure over longer paths from the center to the border of the Paraná Basin.

their model, the thicknesses of the basalt and sedimentary layers were taken into account). Our profiles in Fig. 10 show no evidence of high velocities in the lower crust that might be consistent with underplating/intrusions.

S-wave velocities in the lower crust tend to cluster around 4.0 km/s, with an average  $V_p/V_s$  ratio of 1.78, according to Holbrook et al. (1992). The average ratio for the whole continental crust has been estimated at  $V_p/V_s = 1.77$  (Christensen, 1996). Our measurements of  $V_p/V_s$  ratios in the Paraná Basin (Table 1) do not show any high value trend and may be even lower than the global average. The observed S-velocities lower than 3.8 km/s (Fig. 10) and the normal  $V_p/V_s$  ratios (Table 1) show that no significant layer with high P-wave velocity is present beneath the Paraná Basin that could be attributed to lower crust densification.

Similar conclusions were drawn by An and Assumpção (2004) on the basis of the S-velocity profiles beneath each of the three stations at the basin center (POPB, PACB, PPDB), which show no evidence of significant high velocities in the lowermost crust except for a transitional Moho beneath POPB. Surface-wave tomography of the South American continent (Feng et al., 2004) also indicates lower average S-wave velocities at 30 km depth beneath the Paraná Basin relative to the high velocities in the surrounding foldbelts. Possible underplating processes accompanying the Mesozoic South Atlantic rifting were not widespread in the Paraná Basin; they may have been limited and not detectable by our studies or localized closer to the Atlantic margin.

Our results favor subsidence mechanisms that do not require extensive lower crust densification/underplating, such as flexural effects from nearby orogenies or upper mantle flow. If the phases of rapid subsidence were caused by extensional processes (Quintas et al., 1999), the stretching factors were

probably too small (Fig. 1a) to cause detectable lower crust intrusions.

Other interpretations of the high Bouguer anomalies near the basin axis must be sought, such as a higher density lithospheric upper mantle. The generally thicker crust in the middle of the Paraná Basin compared with the surrounding foldbelts (Assumpção et al., 2002) suggests that the source of the gravity anomaly might be a higher density upper mantle. Rayleigh-wave group velocity tomography (Feng et al., 2004) indicates high upper mantle velocities beneath the middle of the Paraná Basin at 100–150 km depth. Fig. 10 also hints at the possibility of higher velocities below 100 km in the middle of the basin, compared with the basin average, but this difference is not significant with the presently available data.

## 9. Conclusion

Determination of crustal structure with surface waves can make a valuable contribution to studies of the evolution of the Paraná Basin.

Surface wave dispersion can be inverted more efficiently with a GA coupled with a local trial-and-error jumping iteration. This HGA is less sensitive to the initial models, population size, and search resolution. Synthetic tests show that our HGA finds the optimum solution and the range of acceptable models. Inclusion of the Ps–P constraint has a limited effect on the general trend of the S-velocity profile but helps decrease the range of acceptable models and better define the Moho depths.

The S-wave models for the average RIFB paths, inverted by HGA, confirm previous results obtained with LLSI and NA. The results for the long path POPB–CANB are consistent with the RIFB paths. Their models may represent the approximate average structure of the whole Paraná Basin. However, synthetic tests show that strong lateral variations along the path can cause artificial effects in the inverted models, such as overly high velocity in the lithospheric lid. Taking these uncertainties into account, no significant difference is observed in the upper mantle structure between the various profiles. The average S-wave velocity in the upper mantle beneath the Paraná Basin is 4.65 km/s, a typical value for stable platform areas.

S-velocities in the lower crust throughout the Paraná Basin are less than 3.8 km/s, lower than the global average, which confirms prior results reported by An and Assumpção (2004) and Feng et al. (2004). No high velocities are detected in the lower crust that could be caused by significant, widespread magmatic intrusions or underplating. Our results favor subsidence mechanisms that do not require significant amounts of lower crust densification.

## Acknowledgements

This work was financed by grants 00/07134-2 and 01/06066-6 (FAPESP-Brazil) and 30.0227/79 (CNPq-Brazil). The authors thank Robert B. Herrmann and Arthur Snoke for discussions on various aspects of surface wave processing.

They thank José Roberto Barbosa for installing and collecting data for all BLSP95 stations. They appreciate suggestions from the reviewers and editor to improve the text.

## References

- Almeida, F.F.M., Brito Neves, B.B., Carneiro, C.D.R., 2000. The origin and evolution of the South American platform. *Earth-Sci. Rev.* 50, 77–111.
- An, M., Assumpção, M., 2004. Multi-objective inversion of surface waves and receiver functions by competent genetic algorithm applied to the crustal structure of the Paraná basin, SE Brazil. *Geophys. Res. Lett.* 31 (5), L05615. doi:10.1029/2003GL019179.
- An, M., Assumpção, M., 2005. Average shallow structure in the Paraná sedimentary basin from surface wave dispersion: effect of lateral variation and different model parameterization. *J. Seismology* 9, 449–462.
- An, M., Shi, Y., 1996. Dynamic genetic algorithms inversion of earthquake focal mechanism from P waves first motions (in Chinese). *Earthquake Res China* 12 (4), 394–402.
- Assumpção, M., James, D.E., Snoke, J.A., 2002. Crustal thickness in SE Brazilian shield by receiver function analysis: implications for isostatic compensation. *J. Geophys. Res.* 107 (B1), 2006. 10.1029/2001JB000422.
- Bhattacharya, S.N., 1983. Higher order accuracy in multiple filter technique. *Bull. Seism. Soc. Am.* 73, 1395–1406.
- Bizzi, L.A., Schobbenhaus, C., Gonçalves, J.H., Baars, F.J., Delgado, I.M., Abram, M.B., Neto, R.L., Matos de., G.M.M., Santos, J.O.S., 2001. Geology, tectonics and mineral resources of Brazil: Geographic information system—gis and maps at the 1:2,500,000 scale. CPRM, Brasília.
- Brito Neves, B.B., Cordani, U.G., 1991. Tectonic evolution of South America during the Late Proterozoic. *Precambrian Res.* 53, 23–40.
- Christensen, N.I., 1996. Poisson's ratio and crustal seismology. *J. Geophys. Res.* 101 (B2), 3139–3156.
- Cordani, U.G., Brito Neves, B.B., Fuck, R.A., Porto, R., Filho, A.T., Cunha, F.M.B., 1984. Estudo preliminar de integração do pré-Cambriano com os eventos tectônicos das bacias sedimentares brasileiras. *Rev. Ciência Técnica Petróleo*, 15. Petrobrás, CENPES, Rio de Janeiro.
- Deb, K., 1998. Genetic algorithm in search and optimization: the technique and applications. In: *Proceedings of International Workshop on Soft Computing and Intelligent Systems*. Machine Intelligence Unit, Indian Statistical Institute, Calcutta, India, pp. 58–87.
- Du, Z.J., Foulger, G.R., 1999. The crustal structure beneath the northwest Fjords, Iceland, from receiver functions and surface waves. *Geophys. J. Int.* 139, 419–432.
- Du, Z.J., Foulger, G.R., Julian, B.R., Allen, R.M., Nolet, G., Morgan, W.J., Bergsson, B.H., Erlendsson, P., Jakobsdottir, S., Ragnarsson, S., Stefansson, R., Vogfjord, K., 2002. Crustal structure beneath western and eastern Iceland from surface waves and receiver functions. *Geophys. J. Int.* 149, 349–363.
- Durrheim, R.J., Mooney, W.D., 1994. Evolution of the Precambrian lithosphere: seismological and geochemical constraints. *J. Geophys. Res.* 99 (B8), 15359–15374.
- Dziewonski, A., Bloch, S., Landisman, M., 1969. A technique for analysis of transient seismic signals. *Bull. Seism. Soc. Am.* 59, 427–444.
- Feng, M., Assumpção, M., Van Der Lee, S., 2004. Group-velocity tomography and lithospheric s-velocity structure of the south american continent. *Phys. Earth Planet. Int.* 147 (4), 315–331. doi:10.1016/j.pepi.2004.07.008.
- França, G.S.L., 2003. Estrutura da Crosta no Sudeste e Centro-Oeste do Brasil, Usando Função do Receptor (PhD thesis). IAG, Universidade de São Paulo, São Paulo, Brazil.
- França, G.S., Assumpção, M., 2004. Crustal structure of the Ribeira fold belt, SE Brazil, derived from receiver functions. *J. South Am. Earth Sci.* 16 (8), 743–758.
- Goldberg, D.E., Voessner, S., 1999. Optimizing global-local search hybrids. In: Banzhaf, W., Daida, J., Eiben, A.E., Garzon, M.H., Honavar, V., Jakiela, M., Smith, R.E. (Eds.), *GECCO'99: Proceedings of the Genetic and Evolutionary Computation Conference (1)*. Morgan Kaufmann, San Francisco, CA, pp. 220–228.

- Goldberg, D.E., Deb, K., Clark, J.H., 1992. Genetic algorithms, noise, and the sizing of populations. *Complex Syst.* 6, 333–362.
- Herrin, E., Goforth, T., 1977. Phase-matched filters: application to the study of Rayleigh waves. *Bull. Seism. Soc. Am.* 67, 1259–1275.
- Herrmann, R.B., 1973. Some aspects of band-pass filtering of surface waves. *Bull. Seism. Soc. Am.* 63, 663–671.
- Herrmann, R.B., 1987. *Computer Programs in Seismology*. St Louis University, St Louis, MO.
- Herrmann, R.B., 2001. *Computer Programs in Seismology—an Overview of Synthetic Seismogram Computation*. St. Louis University, St Louis, MO.
- Herrmann, R.B., Ammon, J.C., 2002. *Computer Programs in Seismology—Surface Waves, Receiver Functions and Crustal Structure*. St. Louis University, St Louis, MO.
- Holbrook, W.S., Reiter, E.C., Purdy, G.M., Toksoz, M.N., 1992. Image of the Moho across the continent-ocean transition, US east coast. *Geology* 20, 203–206.
- Julià, J., Ammon, C.J., Herrmann, R.B., Correig, A.M., 2000. Joint inversion of receiver function and surface wave dispersion observations. *Geophys. J. Int.* 143, 99–112.
- Levshin, A.L., Ritzwoller, M.H., Barmine, M.P., Ratnikova, L.I., Padgett, C.A., 1998. Automated surface wave analysis using phase-matched filters from dispersion maps. In: *Proceedings of the 20th Seismic Research Symposium on Monitoring a CTBT*, pp. 466–473.
- Ligorria, J.P., Ammon, C.J., 1999. Iterative deconvolution and receiver-function estimation. *Bull. Seism. Soc. Am.* 89, 1395–1400.
- Lomax, A., Snieder, R., 1994. Finding sets of acceptable solutions with a genetic algorithm with application to surface wave group dispersion in Europe. *Geophys. Res. Lett.* 21, 2617–2620.
- Lomax, A., Snieder, R., 1995. The contrast in upper mantle shear-wave velocity between the East European Platform and tectonic Europe obtained with genetic algorithm inversion of Rayleigh-wave group dispersion. *Geophys. J. Int.* 123, 169–182.
- Milani, E.J., Ramos, V.A., 1998. Orogenias Paleozóicas no domínio sul-ocidental do Gondwana e os ciclos de subsidência da bacia do Paraná. *Revista Brasileira de Geociências* 28 (4), 473–484.
- Milani, E.J., Thomaz Filho, A., 2000. Sedimentary basins of South America. In: Cordani, U.G., Milani, E.J., Thomaz Filho A. and Almeida Campos D. de (Eds.), *Tectonic Evolution of South American*. 31st International Geological Congress, Rio de Janeiro, Brazil, pp. 389–449.
- Molina, E.C., Ussami, N., Sá, N.C., Blitkow, D., 1989. Interpretação dos dados gravimétricos da parte norte da bacia do Paraná. *Rev. Bras. Geociências* 19, 187–196.
- Mooney, W.D., Andrews, M.C., Ginzburg, A., Peters, D.A., Hamilton, R.M., 1983. Crustal structure of the Mississippi embayment and a comparison with other continental rift zones. *Tectonophysics* 94, 327–348.
- Mooney, W.D., Coleman, R.G., Reddy, P.R., Artemieva, I., Billien, M., Lévêque, J., Detweiler, S.T., 2001. A review of new seismic constraints of crust and mantle structure from China and India coupled with seismic  $Q_s$  and temperature estimates for the upper mantle. In: *23rd Seismic Research Review: Worldwide Monitoring of Nuclear Explosions*, pp. 90–99.
- Nunn, J.A., Aires, J.R., 1988. Gravity anomalies and flexure of the lithosphere at the Middle Amazon Basin. *J. Geophys. Res.* 93 (B1), 415–428.
- Özalaybey, S., Savage, M.K., Sheehan, A.F., Louie, J.N., Brune, J.N., 1997. Shear-wave velocity structure in the northern basin and range province from the combined analysis of receiver functions and surface waves. *Bull. Seism. Soc. Am.* 87, 183–199.
- Pysklywec, R.N., Quintas, M.C.L., 2000. A mantle flow mechanism for the late Paleozoic subsidence of the Paraná Basin. *J. Geophys. Res.* 105 (B7), 16359–16370.
- Quintas M.C.L., 1995. *O Embasamento da Bacia do Paraná: Reconstrução Geofísica de seu Arcabouço* (PhD thesis), Departamento de Geofísica, IAG-USP, São Paulo, Brazil.
- Quintas, M.C.L., Mantovani, M.S.M., Zalán, P.V., 1999. Contribuição ao estudo da evolução mecânica da Bacia do Paraná. *Rev. Bras. Geociências* 29, 217–226.
- Schaffer, J.D., Caruana, R.A., Eshelman, L.J., Das, R., 1989. A study of control parameters affecting online performance of genetic algorithms for function optimization. In: Schaffer, J.D. (Ed.), *Proceedings of the Third International Conference on Genetic Algorithms*. Morgan Kaufmann, San Mateo, CA, pp. 51–60.
- Schimmel, M., Assumpção, M., VanDecar, J.C., 2003. Upper mantle seismic velocity structure beneath SE Brazil from P- and S-wave travel time inversions. *J. Geophys. Res.* 108 (B4), 2191. doi:10.1029/2001JB000187.
- Shi, Y., Jin, W., 1996. Genetic algorithm inversion of lithospheric structure from surface wave dispersion. *Chinese J. Geophys.* 39 (1), 101–111.
- Snoke, J.A., James, D.E., 1997. Lithospheric structure of the chaco and paraná basins of south america from surface-wave inversion. *J. Geophys. Res.* 102 (B2), 2939–2951.
- Snoke, J.A., Sambridge, M., 2002. Constraints on the s wave velocity structure in a continental shield from surface wave data: comparing linearized least squares inversion and the direct search neighbourhood algorithm. *J. Geophys. Res.* 107 (B5), 2094. 10.1029/2001JB000498.
- Ussami, N., Sá, N.C., Molina, E.C., 1993. Gravity map of Brazil. 2: regional and residual isostatic anomalies and their correlation with major tectonic provinces. *J. Geophys. Res.* 98 (B2), 2199–2208.
- Vidotti, R.M., Ebinger, C.J., Fairhead, J.D., 1998. Gravity signature of the western Paraná basin, Brazil. *Earth and Planetary Science Lett.* 159, 117–132.
- White, R., McKenzie, D., 1989. Magmatism at rift zones: the generation of volcanic continental margins and flood basalts. *J. Geophys. Res.* 94 (B2), 7685–7730.
- Yamanaka, H., Ishida, H., 1996. Application of genetic algorithms to an inversion of surface wave dispersion data. *Bull. Seism. Soc. Am.* 86 (2), 436–444.
- Zalán, P.V., Wolff, S., Conceição, J.C.J., Marques, A., Astolfi, M.A.M., Vieira, I.S., Appi, V.T., Zanutto, O.A., 1990. Bacia do Paraná. In: Gabaglia, G.P.R., Milani, E.J. (Eds.), *Origem e Evolução das Bacias Sedimentares*. Petrobrás, Rio de Janeiro, Brazil, pp. 135–168.
- Zhang, K., Snoke, J.A., James, D.E., 1998. Lithospheric structure of the eastern Paraná basin of central Brazil from surface-wave inversion: comparing genetic algorithms and linearized least-squares inversion. *IRIS Workshop*, Santa Cruz, CA.